

1 Constraints on coronal turbulence models from
2 source sizes of noise storms at 327 MHz

arXiv:1012.3523v2 [astro-ph.SR] 5 Feb 2011

Prasad Subramanian, Indian Institute of Science Education and Research, Sai Trinity Building,
Pashan, Pune - 411021, India. (p.subramanian@iiserpune.ac.in)

Iver Cairns, School of Physics, University of Sydney, NSW 2006, Australia.
(cairns@physics.usyd.edu.au)

Abstract. We seek to reconcile observations of small source sizes in the
solar corona at 327 MHz with predictions of scattering models that incor-
porate refractive index effects, inner scale effects and a spherically diverg-
ing wavefront. We use an empirical prescription for the turbulence ampli-
tude $C_N^2(R)$ based on VLBI observations by Spangler and coworkers of com-
pact radio sources against the solar wind for heliocentric distances $R \approx$
10–50 R_\odot . We use the Coles & Harmon model for the inner scale $l_i(R)$, that
is presumed to arise from cyclotron damping. In view of the prevalent un-
certainty in the power law index that characterizes solar wind turbulence at
various heliocentric distances, we retain this index as a free parameter. We
find that the inclusion of spherical divergence effects suppresses the predicted
source size substantially. We also find that inner scale effects significantly
reduce the predicted source size. An important general finding for solar sources
is that the calculations substantially underpredict the observed source size.
Three possible, non-exclusive, interpretations of this general result are pro-
posed. First and simplest, future observations with better angular resolution
will detect much smaller sources. Consistent with this, previous observations
of small sources in the corona at metric wavelengths are limited by the in-
strument resolution. Second, the spatially-varying level of turbulence $C_N^2(R)$
is much larger in the inner corona than predicted by straightforward extrap-
olation Sunwards of the empirical prescription, which was based on obser-
vations between 10–50 R_\odot . Either the functional form or the constant of pro-

25 portionality could be different. Third, perhaps the inner scale is smaller than
26 the model, leading to increased scattering.

1. Introduction

27 Refractive scattering of radiation by density turbulence in the Sun’s corona and so-
 28 lar wind leads to angular broadening of embedded radio sources, and of cosmic sources
 29 observed through these media. The process is similar to the twinkling of stars and mod-
 30 ified “seeing” caused by density turbulence in Earth’s atmosphere and ionosphere. This
 31 scattering process has been investigated for many years using geometrical optics [e.g.,
 32 Steinberg et al 1971] and the parabolic wave equation [e.g., Lee and Jokipii, 1975; Coles
 33 and Harmon 1989; Bastian 1994; Cairns 1998].

34 Scattering is thought to affect the observed properties of type II and III solar radio
 35 bursts in several ways: greatly increasing the angular sizes of the sources [e.g., Riddle
 36 1974], causing the time profiles to have exponential decreases [e.g., Robinson and Cairns,
 37 1998], and causing anomalously low brightness temperatures at decametric wavelengths
 38 [e.g., Thejappa & Kundu 1992].

39 The primary motivation of this paper is to investigate the constraints imposed on models
 40 of density turbulence in the solar corona by recent observations at 327 MHz [Mercier et al.,
 41 2006], made by combining visibilities from the Giant Metrewave Radio Telescope (GMRT)
 42 in Pune, India, and the Nancay Radioheliograph (NRH) in France. The maps of Mercier
 43 et al. [2006] show structures ranging from the smallest observed size of $49''$ to that of the
 44 whole Sun, with dynamic ranges as high as a few hundred. These features make them the
 45 best meter wavelength snapshot maps of the solar corona to date. Mercier et al. [2006]
 46 found the smallest steady angular size of type I solar noise storms to be $49''$ in their high
 47 dynamic range, full disk, 17 second snapshots. We therefore adopt the smallest observed

48 source size of $49''$ in these maps to be a canonical number for comparison with our model
 49 predictions. The only other two-dimensional map showing small source sizes that we are
 50 aware of is that of Zlobec et al [1992], who observed a source as small as $30''$ at 327 MHz.
 51 However, the dynamic range of their map was severely limited, and included only a very
 52 small range of size scales. It should be noted that the lower limit to the observed size is
 53 imposed by the resolution of the instrument if scattering by density turbulence is weak
 54 enough. The scattering calculations shown below imply that there is a possibility that
 55 smaller solar sources will be detected in the future by instruments with improved angular
 56 resolution.

57 In this paper we use a formalism based on the paraxial wave equation and the structure
 58 function, together with observationally based models for the density turbulence that scat-
 59 ter the radiation, to predict the size of sources in the solar corona at 327 MHz. Our results
 60 can be interpreted as the scatter-broadened image of an ideal point source in the solar
 61 corona. We have used an empirical model for the amplitude $C_N^2(R)$ of coronal turbulence
 62 that is based directly a fit to the scattering measure obtained from VLBI observations of
 63 cosmic sources broadened by scattering in the outer solar corona and inner solar wind.
 64 Here R is the heliocentric distance. We have assumed that this model is valid through-
 65 out the corona, specifically at smaller R . We also consider the effects of spherical and
 66 plane wave propagation, variations of the inner scale $l_i(R)$ and power-law index α of the
 67 turbulence on the predicted source sizes. In most cases, we find that the models predict
 68 sizes that are at least an order of magnitude below the smallest observed size of $49''$ at
 69 327 MHz. Our formalism and analyses differ primarily from those of Bastian [1994] in the
 70 models for $C_N^2(R)$ and the electron density profile $n_e(R)$, while our applications are to

metric rather than centimetric and decimetric emissions. Since our predictions are much smaller and Bastian's [1994] predictions much larger than $49''$ at 327 MHz, the analyses demonstrate the importance of knowing $C_N^2(R)$, $n_e(R)$, and $l_i(R)$ much better for future observations and predictions of solar sources. These quantities are also relevant to the heating and outward flow of the coronal plasma, with activity localized to specific ranges of R potentially leading to larger $C_N^2(R)$ and so enhanced scattering at, say, decimetric frequencies than expected at, say, metric frequencies.

The paper is organized as follows. In § 2 we summarize the scattering formalism and observations of the density turbulence. Coronal density models are described in § 3. The results are presented in § 4, including estimates of the predicted angular broadening, and the implications for coronal density turbulence. The conclusions are presented in § 5.

2. Angular broadening

We first consider the angular broadening predicted by the empirical formula of Erickson (1964):

$$\theta = 50 \left(\frac{\lambda}{D} \right)^2 \text{ arcminutes} . \quad (1)$$

Here λ is the observing (free-space) wavelength in meters and D is the elongation in units of R_\odot . If we take $D = 1.056R_\odot$, which is where 327 MHz emission would originate according to the hybrid density model described below, then $\theta \simeq 50'$ for 327 MHz, which is much larger (60 times) than the observed $49''$. It points to a significant difference between the situation for observations of celestial background sources against the solar wind, for which Erickson's (1964) formula is well accepted, and observations of solar radio events

88 that originate in the solar corona. This difference will be specifically addressed in the
 89 Discussion section below.

2.1. Density turbulence

Density turbulence in the Sun's corona and solar wind is modeled here by writing the three-dimensional isotropic spatial power spectrum $S_n(k, R)$ of the fluctuating part δn of the electron density n_e as [cf., Lee & Jokipii 1975; Rickett 1977; Coles and Harmon, 1989; Bastian, 1994; Cairns 1998; Spangler, 2002]

$$S_n(k, R) = \langle (\delta n)^2 \rangle(k, R) = C_N^2(R) k^{-\alpha} e^{-k^2/q_i^2} . \quad (2)$$

90 Here k and R are the (isotropic) wavenumber and radial distance (in units of R_\odot), re-
 91 spectively, $C_N^2(R)$ models the level of turbulence, α is the power-law index, and q_i is the
 92 wavenumber corresponding to the inner scale of the turbulence. While it is fairly well
 93 established that the turbulence spectrum largely follows the Kolmogorov scaling (with
 94 $\alpha = 11/3$) at scales larger than about 100 km, there is some evidence that it flattens,
 95 with α decreasing to values as low as 3, at scales between a few km and a few hundred
 96 km [Bastian, 1994]. There is also some evidence for variation of the turbulence power
 97 law spectrum with heliocentric distance [e.g., Efimov et al., 2008]. Furthermore, there
 98 is evidence for significant variation in the index between the slow and fast solar wind
 99 [Manoharan et al., 1994]. We therefore retain α as a parameter. It may be noted that
 100 some authors use a power law index of 5/3 to describe the one-dimensional Kolmogorov
 101 spectrum; the index they refer to is equal to $\alpha - 2$.

The empirical model we use for $C_N^2(R)$ was originally mooted by Armstrong & Woo [1980] and later refined, based on VLBI observations between 10–50 R_\odot , by Spangler &

Sakurai [1995] and Spangler [2002] among others:

$$C_N^2(R) = 1.8 \times 10^{10} \left(\frac{R}{10R_\odot} \right)^{-3.66} . \quad (3)$$

102 The dimensions of C_N^2 depend on α , being $\text{m}^{-\alpha-3}$. The normalizations for C_N^2 differ by
 103 about a factor of a few and the power-law index with R ranges from -3.66 to -4 in these
 104 works, presumably due to solar wind variability.

The inner scale l_i is modeled using Coles & Harmon's [1989] model which agrees roughly with their observations,

$$q_i(R) = \Omega_i(R)/3V_A(R) \equiv 2\pi/l_i(R) = \frac{2\pi}{684 n_e(R)^{-1/2}} \text{ km}^{-1} \quad (4)$$

105 where Ω_i is the ion cyclotron frequency, V_A is the Alfvén speed and n_e is the electron
 106 density in cm^{-3} . This model is interpreted conventionally in terms of cyclotron damping
 107 by MHD waves. We use this definition for the inner scale throughout this paper, except
 108 in two cases where we artificially set l_i equal to a very small value.

109 A popular alternative prescription for C_N^2 supposes that C_N^2 is \propto the square of the
 110 background electron density. Such a prescription has a constant of proportionality, which
 111 is often determined via observed values of the phase structure function (e.g., Bastian
 112 1994). The magnitude of the phase structure function in turn, is very dependent on the
 113 elongation to which it is referenced. We discuss this issue further in § 4.

2.2. Plane vs spherical wave propagation

114 Scattering depends quantitatively on whether the wavefront is planar (1-D) or spherical
 115 (3-D). When a source is embedded in the scattering medium, it is often appropriate to
 116 adopt a formalism that includes the spherically diverging nature of the wavefront. The
 117 geometry for spherically diverging propagation is shown in Figure 1.

Figure 1

Similarly, when a plane wave illuminates the scattering medium, a 1-D planar formalism is standard. In this case an observer is typically sensitive only to scattering regions (eddies) with sizes of order the baseline length s . In the spherically diverging situation, however, the observer is sensitive to a range of eddy sizes given by sa/b , where a is the (continuously varying) distance of the scattering screen from the source and b is the distance of the observer from the source. In our situation, this is tantamount to saying that the effective baseline for spherical wave propagation is [Ishimaru, 1978]

$$s_{\text{eff}} = sR/(R_1 - R_0). \quad (5)$$

118 This is the basic difference between Eqs (8) and (9) discussed below.

119 In the solar situation, radiation from an embedded coronal source is subject to scat-
 120 tering as it propagates to the observer. Since the radiation is generated near f_p and $2f_p$,
 121 scattering effects are expected to be largest in the source and in its vicinity, assuming
 122 that $f_p(R)$ decreases monotonically with increasing R . Spherical effects are expected to
 123 arise in two ways. Firstly, scattering will maximally distort an initially plane wavefront
 124 close to and in the source. Secondly, on a larger scale, the solar wind density is expected
 125 to be spherically symmetric, with radiation being refracted towards the radial direction.
 126 Accordingly, spherical divergence effects are expected to be vital. They are explicitly
 127 calculated below and shown to be quantitatively important. In contrast, the planar for-
 128 malism is expected to be appropriate when the source, scattering region(s), and observer
 129 are all far apart, as assumed in calculations for pulsars and other celestial sources.

2.3. Structure function

The starting points for the expression we use for the scattering angle are equations (4)–(7) of Coles et al [1987] that specify the structure function and the mutual coherence function using the parabolic wave equation (PWE) formalism that includes small-angle refractive scattering and diffraction, but not reflection. For the sake of completeness, we reproduce them below. The asymptotic forms of the gradient of the phase structure function $D(s, R)$ are

$$\frac{\partial}{\partial R} D(s, R) = \frac{8\pi^2}{2^{\alpha-2}(\alpha-2)} \frac{\Gamma(1 - (\alpha-2)/2)}{\Gamma(1 + (\alpha-2)/2)} C_N^2(R) r_e^2 \lambda^2 s^{\alpha-2}, \quad \text{for } s_{\text{eff}} \gg l_i(R), \quad (6)$$

$$\frac{\partial}{\partial R} D(s, R) = \frac{4\pi^2}{2^{\alpha-2}} \Gamma\left(1 - \frac{(\alpha-2)}{2}\right) C_N^2(R) r_e^2 \lambda^2 l_i(R)^{\alpha-4} s^2, \quad \text{for } s_{\text{eff}} \ll l_i(R), \quad (7)$$

130 where r_e is the classical electron radius, λ is the observing wavelength and s_{eff} is the
 131 effective interferometer spacing. It is noted that this formalism is valid only for $2 < \alpha < 4$;
 132 in particular, equations (6) and (7) diverge at $\alpha = 4$ owing to the behavior of the term
 133 $\Gamma(1 - (\alpha - 2)/2)$. It may also be noted that the branches (6) and (7) do not meet at
 134 $s_{\text{eff}} = l_i$; the ratio of (7) to (6) is equal to $(1/2)(\alpha - 2) (l_i/s)^{\alpha-4} \Gamma(1 + (\alpha - 2)/2)$, and at
 135 $s_{\text{eff}} = l_i$ this is equal to unity only for $\alpha = 4$.

The effective interferometer spacing s_{eff} is equal to s for the case of plane wave propagation, but is equal to $sR/(R_1 - R_0)$ for spherical wave propagation, as discussed in § 2.2 and Figure 1. The phase structure function for the cases of plane wave and spherical wave propagation are

$$D_p(s) = \int_{R_0}^{R_1} \frac{\partial}{\partial R} D(s, R) dR, \quad \text{for plane wave propagation,} \quad (8)$$

$$D_s(s) = \int_{R_0}^{R_1} \frac{\partial}{\partial R} D\left(\frac{sR}{R_1 - R_0}, R\right) dR, \quad \text{for spherical wave propagation,} \quad (9)$$

136 where the lower limit of integration R_0 is the radial distance from which scattering is
 137 assumed to be effective (we take this to be equal to the fundamental emission level), and
 138 the upper limit R_1 corresponds to the observer (here at $R_1 = 1$ AU). All quantities are
 139 assumed to have spherical symmetry and the path is assumed to be radial.

Scattering depends sensitively on the ratio of the radiation frequency f to the local electron plasma frequency $f_p(R)$ [Cairns, 1998]. Equations (16) and (22) of Cairns [1998] include the effects on refractive scattering that arise from $f_p(R)$ being non-zero and varying with position between the source and observer. By analogy with these equations we write

$$D_{pf}(s) = \int_{R_0}^{R_1} \frac{1}{1 - f_p(R)^2/f^2} \frac{\partial}{\partial R} D(s, R) dR \quad (10)$$

for plane wave propagation and

$$D_{sf}(s) = \int_{R_0}^{R_1} \frac{1}{1 - f_p(R)^2/f^2} \frac{\partial}{\partial R} D\left(\frac{sR}{R_1 - R_0}, R\right) dR \quad (11)$$

140 for spherical wave propagation, respectively.

The scattering angle is conventionally defined using a coherence scale s_0 in the following manner [e.g., Coles et al., 1987; Bastian, 1994]:

$$\theta_c = (2\pi s_0/\lambda)^{-1}, \quad (12)$$

where

$$D_*(s_0) = 1 \quad (13)$$

141 and $D_*(s)$ is either equal to $D_{pf}(s)$, defined by (10), or $D_{sf}(s)$, defined by (11), in ap-
 142 propriate limits. This scattering angle θ_c can be interpreted as the predicted size of an
 143 idealized point source.

2.4. Density Models

A model for $n_e(R)$ in the corona and solar wind is required to be able to predict the angular broadening. The density model is required for computing the inner scale, which is defined in the next subsection. Since there is no universally accepted model, we initially consider four representative density models. One is the four-fold Newkirk density model for the corona, based on eclipse observations [Newkirk, 1961]:

$$n_{4n}(R) = 4 \times 4.2 \times 10^4 \times 10^{4.32/R} \quad \text{cm}^{-3}, \quad (14)$$

The second model is derived from the frequency drift rate of interplanetary type III bursts [Leblanc et al., 1998]:

$$n_{\text{lb}}(R) = 3.3 \times 10^5 R^{-2} + 4.1 \times 10^6 R^{-4} + 8 \times 10^7 R^{-6} \quad \text{cm}^{-3}. \quad (15)$$

The third model considered is due to Aschwanden et al. [1995]. It is based on the drift rates of type III bursts [Alvarez & Haddock, 1973] in the outer corona and solar wind ($f < 10$ MHz) and assumes an isothermal barometric atmosphere for the lower corona:

$$n_a(R) = \begin{cases} n_1 \left(\frac{R-1}{R_2} \right)^{-p}, & R > 1 + R_2 \\ n_Q \exp \left(-\frac{R-1}{\mu} \right), & R < 1 + R_2 \end{cases} \quad (16)$$

where $p = 2.38$, $n_Q = 4.6 \times 10^8 \text{ cm}^{-3}$, $n_1 = n_Q \exp(-p)$, $\mu = 0.1$ and $R_2 = p\mu$. The fourth model is a ‘‘hybrid’’, using the Aschwanden & Benz [1995] model for the lower corona and the four-fold Newkirk model multiplied by a normalization factor (to ensure continuity) in the upper corona. In other words, the density $n_{\text{hyb}}(R)$ of the hybrid model is

$$n_{\text{hyb}}(R) = \begin{cases} A n_{4n}(R), & R > 1 + R_2 \\ n_a(R), & R < 1 + R_2, \end{cases} \quad (17)$$

¹⁴⁴ where $A = 0.324$ is the normalization factor that ensures continuity.

145 Figure 2 shows $f_p(R) = 8.97 n_e(R)^{1/2}$ kHz for all four density models, with n_e in units
 146 of cm^{-3} .

147 The figure shows that the highest frequency predicted for $R > 1$ by the Leblanc et al.
 148 [1998] density model (Eq 15) is less than 100 MHz. Since our observing frequency is 327
 149 MHz, this model is therefore unsuitable for our purposes. However, the four-fold Newkirk
 150 model (14), Aschwanden & Benz [1995] model (16), and hybrid model can account for
 151 $f_p = 327$ MHz for $R > 1$. However, since the Aschwanden & Benz [1995] model predicts
 152 unrealistically low densities (and consequently f_p) for $R > 1 + R_2 = 1.23$, only the hybrid
 153 model is considered further below. Fundamental emission at 327 MHz emanates from
 154 a heliocentric distance of $1.055 R_\odot$ with this model. In order to avoid the singularity
 155 in the integrand in Eqs (10) and (11), we start the integration at $R_0 = 1.056 R_\odot$. In
 156 other words, we start the integration from a distance of approximately 700 km above
 157 the height at which 327 MHz fundamental emission originates. This distance is smaller
 158 than that corresponding to the frequency difference Δf between the minimum frequency
 159 of fundamental emission at a given location and the local value of f_p , so that avoiding
 160 the singularity is correct. This positive frequency difference exists because conservation
 161 of energy and the wave dispersion relations force the standard nonlinear Langmuir wave
 162 processes for fundamental and harmonic emission to produce radiation of order several
 163 percent above f_p and $2f_p$ [e.g., Cairns, 1987a,b], with the value of $\Delta f/f_p$ depending on
 164 the beam and plasma parameters.

2.5. Inner scale effects

165 We next discuss the need for including inner scale effects in our treatment. In general,
 166 inner scale effects are important if the baseline is smaller than the inner scale.

167 Figure 3 shows the inner scale (in km) given by Eq (4), as a function of heliocentric
 168 distance for some of the density models discussed in the preceding section. Clearly, the
 169 inner scale is quite dependent upon the density model. The inner scale for the Aschwanden
 170 & Benz [1995] model far exceeds those for the other models, since the density with this
 171 model for $R > 1.23$ is unrealistically low; we have therefore chosen not to depict the l_i
 172 for this model in Figure 3. As explained in the preceding section, we choose to use only
 173 the hybrid model from now on, for it is by far the most realistic one.

174 In order to ascertain the importance of inner scale effects, we compare l_i with the longest
 175 baseline (that determines the smallest source size), assuming that the source is situated
 176 at the fundamental emission level for 327 MHz, and the observer is at 1 AU. In order
 177 to compute the longest baseline, we set $49'' = 1.22\lambda/s$, where $49''$ is the observed source
 178 size and λ is the (free space) observing wavelength (1 meter). This yields an effective
 179 baseline of $s \sim 5$ km. In order to ascertain the relevance of the inner scale (i.e., whether
 180 we should be using Eq 6 or 7) we need to compare the effective longest baseline s_{eff} with
 181 the inner scale. It may be noted that a typical interferometer measurement involves a
 182 range of baselines, and while the longest baseline we have computed above is the one that
 183 limits the smallest observable source size, baselines shorter than this one do contribute
 184 to the overall measurement. However, our approach is appropriate because the longest
 185 baseline for a given source size is the largest length scale at which there is appreciable
 186 power. Inner scale effects are relevant only for the branch for which the baseline is \ll the
 187 inner scale, as in Eq 7. If the *longest* relevant baseline is smaller than the inner scale, then
 188 it follows that the rest of the baselines in the problem automatically satisfy this criterion.
 189 Our approach thus provides a useful estimate of the importance of inner scale effects.

190 As discussed above, $s_{\text{eff}} = s$ for plane wave propagation, while $s_{\text{eff}} = sR/(R_1 - R_0)$ for
 191 spherical wave propagation. We show the ratio of s_{eff} to l_i in Figure 4.

Figure 4

192 When considering plane wave propagation, $s_{\text{eff}} = s$, and the solid line in Figure 4
 193 shows that s_{eff} is mostly $> l_i$. For heliocentric distances greater than about $30 R_{\odot}$, s_{eff}
 194 does become somewhat smaller than l_i , but most of the contribution to the scattering
 195 kernel arises from distances well inside $30 R_{\odot}$. We should therefore use Eqs (6) and
 196 (10) for plane wave propagation. On the other hand, when considering spherical wave
 197 propagation, $s_{\text{eff}} = sR/(R_1 - R_0)$, and the dotted line in Figure 4 shows that s_{eff} is $< l_i$
 198 for all R . The appropriate equations to use for spherical wave propagation are therefore
 199 Eqs (7) and (11).

3. Results

3.1. Plane wave propagation

200 We first consider plane wave propagation, which is more appropriate for waves emanat-
 201 ing from a background object that is far from the scattering medium.

3.1.1. $s_{\text{eff}} \gg l_i$

203 Since Figure 4 shows that $s_{\text{eff}} > l_i$ for plane wave propagation for $R < 30R_{\odot}$, the
 204 appropriate branch to use is Eq (6). At heliocentric distances greater than about $30 R_{\odot}$,
 205 s_{eff} becomes marginally less than the inner scale, but we have verified numerically that
 206 this is immaterial, since most of the contribution to θ_c takes place well within $30 R_{\odot}$.

207 Figure 5 uses Eqs (6), (10) and (13) to predict the scattering angle $\theta_c(1 \text{ AU})$ at the
 208 Earth, in arcseconds, as a function of the power law index α for plane wave propagation
 209 at $f = 327 \text{ MHz}$. The thin line is for fundamental emission and the thick line is for second
 210 harmonic emission. Removal of the refractive index effect in Eq (10), meaning the factor

Figure 5

211 of $(1 - f_p^2/f^2)^{-1}$, causes a negligible change in the result. The predicted source size is
 212 slightly smaller for second harmonic emission.

213 3.1.2. $s_{\text{eff}} \ll l_i$

214 Although Figure 4 demonstrates that $s_{\text{eff}} > l_i$ for plane wave propagation, we never-
 215 theless investigate the predicted scattering angle for plane wave propagation, while using
 216 branch (7). The results are shown in Figure 6.

Figure 6

217 Evidently, the source sizes predicted approach the observed size for relatively steep
 218 turbulence spectra; for spectra that are steeper than Kolmogorov (i.e., $\alpha > 11/3$), the
 219 predicted source sizes exceed the observed one. In order to investigate inner scale effects
 220 we compute the scattering angle for plane wave propagation with the inner scale set to
 221 an artificially low value of 1 m, instead of being computed self-consistently from Eq 4.
 222 The results are shown using the heavy lines in Figure 7. When inner scale effects are thus
 223 removed, it is clear that the predicted source size increases, especially for flatter spectra.

Figure 7

3.2. Spherical wave propagation

224 As discussed earlier, spherical wave propagation is appropriate when the source is em-
 225 bedded in the scattering medium, as is the case here.

226 3.2.1. $s_{\text{eff}} \ll l_i$

227 Since Figure 4 shows that $s_{\text{eff}} \ll l_i$ for spherical wave propagation, the appropriate
 228 branch to use is (7).

229 The solid line in Figure 7 predicts $\theta_c(1 \text{ AU})$ for spherical wave propagation, using (7),
 230 (10) and (13). Clearly, the predicted scattering angle is at least 25 times smaller than
 231 the observed one. The dashed line, on the other hand, is computed by artificially setting
 232 $l_i = 1\text{m}$, while still using (7). This is tantamount to neglecting inner scale effects. We

233 observe that for flat spectra, inner scale effects substantially reduce (by over an order
 234 of magnitude) the predicted θ_c , but that this difference is progressively reduced as α
 235 increases. There are negligible differences between the results for fundamental and second
 236 harmonic emission, and removal of the refractive index effect causes a negligible change
 237 too.

238 **3.2.2. $s_{\text{eff}} \gg l_i$**

239 In keeping with the spirit of our treatment for plane wave propagation, we investigate
 240 the predicted scattering angle for spherical wave propagation while using branch (6),
 241 which assumes that $s_{\text{eff}} > l_i$. We do this despite Figure 4's prediction that s_{eff} is $< l_i$ for
 242 spherical wave propagation.

243 The difference between fundamental and second harmonic emission are negligible.

244 **3.2.3. Spherical vs plane wave propagation**

245 Although we have investigated several different cases, our attention has been focussed
 246 mainly on two issues: first, the difference between the source sizes predicted for plane
 247 wave and spherical wave propagation, and, second, the influence of the inner scale. We
 248 now compare the plane wave and spherical wave results directly in Figure 9, assuming
 249 fundamental emission, and employing an inner scale that is computed self-consistently
 250 using Eq (4).

251 It is clearly evident from Figure 9 that spherical divergence effects decrease the predicted
 252 scattering angle by around two orders of magnitude as compared to the plane wave case.
 253 This is best seen by comparing the same branch (say, $s_{\text{eff}} > l_i$) for the plane wave and
 254 spherical wave cases. Thus, spherical divergence effects should be quantitatively important
 255 for scattered solar radio emission and plane wave results should be used with great caution.

Figure 9

4. Discussion and Summary

256 The highest resolution meter wavelength observations of the solar corona reveal com-
 257 pact sources around $49''$ in size at 327 MHz. The main aim of this paper is to employ
 258 an observationally-motivated model for the turbulence amplitude C_N^2 , and see what it
 259 implies for the predicted scattering angle for radio sources located in the solar corona.
 260 We reference our calculations to the same frequency (viz. 327 MHz) at which the small-
 261 est source size is observed. We employ the parabolic wave equation, together with the
 262 standard asymptotic forms for the phase structure function, which are valid for situations
 263 where the effective baseline is either much larger or much smaller than the inner scale.
 264 We define the predicted scattering angle θ_c via Eq. (12) as the angle where the phase
 265 structure function falls to $1/e$ times its peak value. Effectively, this means that the scat-
 266 tering angles predicted here should be interpreted as the scatter-broadened image of an
 267 ideal point source in the solar corona. The real source will have an intrinsic size (i.e., it
 268 will not be a point source) and the observable source will be the convolution of the in-
 269 trinsic source profile with θ_c , provided there are no instrumental limitations. The results
 270 in this paper should therefore be regarded as lower limits to the observable source size
 271 set by scattering. The general consensus now seems to be that there is not much about
 272 the intrinsic source size that can be gleaned from scatter-broadened images [Bougeret &
 273 Steinberg, 1977; Melrose, 1980; Bastian, 1994]. However, if the intrinsic source size and θ_c
 274 are similar in size, then the observed source size will be larger than θ_c by a factor near $\sqrt{2}$.
 275 Note that this factor cannot account for the large discrepancies between the minimum
 276 source size observed at 327 MHz [Mercier et al., 2006] and those predicted here. If, on

277 the other hand, the intrinsic source size is much larger, then scatter broadening does not
278 play a significant role.

279 We have included refractive index effects that can be important when the radiation is
280 emitted near the fundamental plasma level, but found them to be relatively unimportant.
281 The inner scale is included via the Coles and Harmon [1986] model, interpreted in terms
282 of cyclotron damping of MHD waves, and so depends primarily on the ambient electron
283 density. We employ a hybrid model for the electron density that yields reasonable heights
284 for meter wavelength emission at the fundamental. In view of the uncertainty in its value
285 in the inner corona, the power law index α characterizing the turbulent spectrum is taken
286 to be a free parameter. We consider both plane wave and spherical wave propagation.
287 For the geometry we consider, where the source is embedded in the scattering medium,
288 the spherical wave description is arguably more appropriate.

289 We have thus explored a wide variety of effects. We observe that there is no significant
290 difference in the predicted scattering angle between fundamental and second harmonic
291 emission. We also find that the removal of the refractive index effect causes a negligible
292 change in the predicted scattering angle. We find that the spherical divergence effect
293 results in a significant lowering of the predicted scattering angle (by around 2 orders of
294 magnitude). We find that removing inner scale effects by artificially setting the inner
295 scale to be equal to a very small value (instead of determining it self-consistently from
296 Eq 4) results in a significant enhancement of the predicted source size. The enhancement
297 is greatest for flatter spectra, where it can be a factor of around 50, and it progressively
298 disappears for steeper spectra.

299 As mentioned earlier, the power law index of the turbulent spectrum is a free parameter.
 300 There is a formal divergence at $\alpha = 4$ in Eqs (6) and (7), and we therefore limit the
 301 computations to a maximum value of $\alpha = 3.97$. The maximum value of the predicted
 302 scattering angle thus occurs at $\alpha = 3.97$.

303 For plane wave propagation, the predicted source size for Kolmogorov turbulence is
 304 around $10''$ lower than the observed one. For spherical wave propagation, we find that
 305 the maximum value of the predicted scattering angle is at least 25 times smaller than
 306 the observed one. It is emphasized that plane wave propagation is relevant to the well-
 307 accepted empirical formula of Erickson [1964], which predicts large source sizes, since it
 308 pertains to observations of celestial sources through the solar wind. Even so, with current
 309 estimates of $l_i(R)$ implying that $s_{\text{eff}} > l_i$ (Figure 4), additional scattering is required to
 310 bring Erickson's result into quantitative agreement with the calculations here for plane
 311 wave scattering. Alternatively, the inner scale $l_i(R)$ should be smaller than that predicted
 312 by the Coles and Harmon [1989] model assumed here, so that $s_{\text{eff}} < l_i$.

313 The crucial result of this paper is that the predicted source sizes are considerably smaller
 314 than the observed lower limit of $49''$ when spherical wave propagation and inner scale
 315 effects are included, as they should be for sources in the solar corona. This broad trend of
 316 the models substantially underpredicting the source size can be interpreted in three ways
 317 that are not exclusive and can occur in combination. First, it could imply that source
 318 sizes much smaller than those that have been observed so far actually exist in the solar
 319 corona, and can potentially be observed. All the instances of observations of small sources
 320 to date have been limited by the instrument resolution; it is therefore quite likely that
 321 smaller sources can be detected when instrument resolutions are improved. Second, this

322 broad trend can be taken to imply that our naive extrapolation of the empirical form for
 323 the turbulence amplitude $C_N^2(R)$ to the inner corona is not justified. The results could
 324 be taken to imply that $C_N^2(R)$ in the inner corona is far higher than suggested by the
 325 empirical formula (3). This could be due to the functional form for $C_N^2(R)$ increasing
 326 more rapidly with decreasing R or due to a larger normalization factor or both effects.
 327 Third, the model (4) may significantly overestimate $l_i(R)$, meaning that the turbulent
 328 cascade extends to smaller length scales (larger q) and leads to more scattering. These
 329 proposals all appear reasonable, and we regard all three as viable.

330 Finally, we discuss the connection between our work and that of Bastian [1994]. The
 331 methodology is similar, and we investigate similar issues such as the effects of the inner
 332 scale, turbulence index α , and spherical versus planar wave propagation. Bastian's [1994]
 333 findings are contrary to ours: we find that our model predictions are substantially below
 334 the minimum observed size of $49''$, while Bastian's [1994] model predictions are substan-
 335 tially above $49''$. Thus, a priori, both models need revision. A major difference is in the
 336 choice of a model for C_N^2 . Bastian [1994] uses a model for C_N^2 which is proportional to
 337 the square of the background electron density and assumes the density model of Riddle
 338 (1974), which also involves a constant of proportionality. These two constants of propor-
 339 tionality are absorbed into one and fixed by normalizing the structure function $D_{20}(10\text{km})$
 340 for a baseline of 10 km, an observing wavelength of 20 cm, and an elongation of $5 R_\odot$. In
 341 contrast, as explained earlier, the C_N^2 model we use is determined by an empirical fit to
 342 VLBI scattering observations between $10\text{--}50 R_\odot$; this was motivated by the need to use
 343 a C_N^2 model that is derived as directly as possible from observations. A minor matter is
 344 that Bastian [1994] discusses the disk to limb variation in the predicted scattering angle,

345 whereas our treatment is valid only for sources that are reasonably close to disk center.
 346 In order to do so, we would need to use the general formalism used here, together with an
 347 integration path that incorporates the appropriate extra path length needed for sources
 348 that are displaced from the disk center.

349 An appropriate means of comparing the normalizations of the two treatments is thus
 350 to compare the normalizations of the structure function. Using (10) – (13), we write the
 351 structure functions as

$$\begin{aligned}
 D_{sf}(s) &= \frac{4\pi^2 s^2}{\lambda^2} \theta_{csf}^2, \\
 D_{pf}(s) &= \left(\frac{2\pi s}{\lambda}\right)^{\alpha-2} \theta_{cpf}^{\alpha-2},
 \end{aligned}
 \tag{18}$$

352 where $\theta_{csf}(s)$ is the value of θ_c for spherical wave propagation using branch (7) and
 353 $\theta_{cpf}(s)$ corresponds to plane wave propagation for branch (6). Then using our models for
 354 $C_N^2(R)$, $l_i(R)$, and $n_{hyb}(R)$ we find that $D_{sf}(s) = 2.8 \times 10^{-3} \text{ rad}^2$ for $s = 10 \text{ km}$, $\lambda = 91 \text{ cm}$
 355 (corresponding to 327 MHz), $\alpha = 11/3$ and a starting height corresponding to 327 MHz
 356 fundamental emission. The same prescription and parameters yield $D_{pf}(s) = 7.7 \times 10^{-3}$
 357 $\text{rad}^{5/3}$. Since the structure functions we derive are based on integrations over heliocentric
 358 distance, we cannot assign a specific elongation to them.

359 In comparison, Bastian normalizes C_N^2 by assuming $D_{20\text{cm}}(10\text{km}) = 4\text{--}12 \text{ rad}^2$, based
 360 on measurements of by Coles and Harmon [1989] and Armstrong et al. [1990] of cosmic
 361 sources (implying primarily planar wave effects) at an elongation of $5 R_\odot$. In order to
 362 normalize Bastian's [1994] values for the structure function to a wavelength of 91 cm,
 363 we concentrate on the structure function for spherical wave propagation. Inspection of
 364 Eqs [11] and [18] reveals that $D_{sf}(s) \propto \lambda^2$. Therefore, $D_{20\text{cm}}(10\text{km})/D_{91\text{cm}}(10\text{km}) = 21$.
 365 Bastian's [1994] range of values for $D_{20\text{cm}}(10\text{km})$ thus corresponds to $D_{91\text{cm}}(10\text{km}) =$

366 $82 - 250 \text{ rad}^2$. The difference in $D_{91\text{cm}}(10\text{km})$ between the two prescriptions is thus a
 367 factor of $\approx (30 - 90) \times 10^3$, corresponding to a factor $\approx 170 - 300$ in θ_c .

368 This large difference $\approx (30 - 90) \times 10^3$ in the normalization of the structure function
 369 is primarily indicative of a corresponding difference in the normalization of C_N^2 between
 370 the two treatments; this is because neglect of inner scale effects increases θ_c by less than
 371 a factor of 10 for Kolmogorov turbulence in Figure 7. In this connection, we note that
 372 Bastian's [1994] normalization for $D_{20\text{cm}}(10\text{km})$ is based on values of $D(s)$ measured at
 373 an elongation of $5 R_\odot$. We also note (e.g., Fig 1 of Coles & Harmon [1989]) that values
 374 of $D(s)$ measured at larger elongations can be considerably lower (by as much as a few
 375 orders or magnitude, depending upon the elongation). This is significant, since the model
 376 for C_N^2 that we use in this paper is based on observations between 10 and $50 R_\odot$.

377 In summary, the foregoing results demonstrate conclusively that spherical wave prop-
 378 agation effects are vital for solar sources, with plane wave predictions several orders of
 379 magnitude larger than the spherical predictions. Similarly, inner scale effects are quan-
 380 titatively important, while fundamental versus harmonic radiation effects are relatively
 381 small. The results and discussion above demonstrate the importance of accurate models
 382 for $C_N^2(R)$ and to a lesser extent models of $l_i(R)$ and $\alpha(R)$. This paper's prescription for
 383 C_N^2 (Eq [3]) is empirical and directly based on observations (but extrapolated to smaller
 384 R), does not have any normalization constants that need to be determined, and leads to
 385 scattered sizes for a point source that are smaller than the minimum source size observed
 386 to date ($49''$ by Mercier et al. [2006]). Thus smaller source sizes than $49''$ may be observ-
 387 able. In contrast, another well-known prescription [Bastian, 1994] predicts much stronger
 388 scattering with source sizes always larger than $49''$: while this is inconsistent with the

389 minimum source size observed to date at 327 MHz, it may provide the extra scattering
 390 required to account for Erickson's empirical angular broadening result for cosmic sources
 391 viewed through the solar wind.

392 While this paper's results extend and confirm previous theoretical results pertaining to
 393 spherical vs. plane wave effects and provide the first explanation of the small source sizes
 394 recently observed, it is also clear that more observational and theoretical work is required
 395 on $C_N^2(R)$ especially, but also on $l_i(R)$ and $\alpha(k, R)$. This includes temporal variations over
 396 the solar cycle but also spatial variations between radio source regions and other regions
 397 of the corona. Increases in $C_N^2(R)$ and decreases in $l_i(R)$ would lead to more scattering.
 398 Work on both $n_e(R)$ and $\delta n(R)/n_e(R)$ may be useful [e.g., Efimov et al., 2008; Cairns et
 399 al., 2009]. It is quite possible that scattering observations and theory will provide useful
 400 constraints on these five quantities and therefore on the processes heating the solar corona
 401 and accelerating the solar wind.

402 **Acknowledgments.**

403 PS acknowledges several illuminating discussions with Prof Rajaram Nityananda. The
 404 authors acknowledge several critical observations made by the anonymous referees, which
 405 have improved the contents of this paper. PS acknowledges support from the Endeav-
 406 our India research fellowship administered by the Department of Education, Science and
 407 Technology, Australian Government, which supported his visit to the University of Syd-
 408 ney. The initial part of this work was carried out when he was at his previous position
 409 at the Indian Institute of Astrophysics. IHC acknowledges the support of the Australian
 410 Research Council.

References

- 411 H. Alvarez and F. T. Haddock (1973), Solar wind density model from km-wave type III
 412 bursts, *Solar Phys.*, *29*, 197–209.
- 413 M. A. Aschwanden and A. O. Benz (1995), Chromospheric evaporation and radio emission
 414 in solar flares, *Astrophys. J.*, *438*, 997–1012.
- 415 J. W. Armstrong and R. Woo (1980), *Rept IOM 3331-80-070*, Jet Propulsion Lab., Cali-
 416 fornia.
- 417 J. W. Armstrong, W. A. Coles, B. J. Rickett and M. Kojima, *Astrophys. J.*, *358*, 685–692.
- 418 T. S. Bastian (1994), Angular scattering of solar radio emission by coronal turbulence,
 419 *Astrophys. J.*, *426*, 774–781.
- 420 J.-L. Bougeret and J.-L. Steinberg (1977), A new scattering process above solar active
 421 regions - Propagation in a fibrous medium, *Astron. Astrophys.*, *61*, 777-783.
- 422 I.H. Cairns (1987a), Fundamental plasma emission by the processes $L \pm S \rightarrow T$, *J. Plasma*
 423 *Phys.*, *38*, 169-178.
- 424 I.H. Cairns (1987b) Second harmonic emission by the processes $L + L \pm S \rightarrow T$, *J. Plasma*
 425 *Phys.*, *38*, 179-198.
- 426 I. H. Cairns (1998), Angular broadening: effects of nonzero, spatially varying plasma
 427 frequency between the source and observer, *Astrophys. J.*, *506*, 456–463.
- 428 I. H. Cairns, V. V. Lobzin, A. Warmuth, B. Li, P. A. Robinson and G. J. Mann (2009),
 429 Direct radio probing and interpretation of the Sun’s plasma density profile, *Astrophys.*
 430 *J.*, *706*, L265 - L269
- 431 W. A. Coles, R. G. Frehlich, B. J. Rickett and J. L. Codona (1987), Refractive scintillation
 432 in the interstellar medium, *Astrophys. J.*, *315*, 666–674.

- 433 W. A. Coles and J. K. Harmon (1989), Propagation observations of the solar wind near
434 the sun, *Astrophys. J.*, *337*, 1023–1034.
- 435 A. I. Efimov, L. N. Samoznaev, M. K. Bird, I. V. Chashei and D. Plettemeier (2008), Solar
436 wind turbulence during the solar cycle deduced from Galileo coronal radio-sounding
437 experiments, *Adv. Space Res.*, *42*, 117–123.
- 438 W. C. Erickson (1964), The radio-wave scattering properties of the solar corona,
439 *Astrophys. J.*, *139*, 1290–1311.
- 440 A. Ishimaru (1978), *Wave Propagation and Scattering in Random Media* (New York:
441 Academic).
- 442 A. Kerdraon, M. Pick, G. Trottet, C. Sawyer, R. Illing, W. Wagner and L. House (1983),
443 The association of radio noise storm enhancements with the appearance of additional
444 material in the corona, *Astrophys. J.*, *265*, L19–L21.
- 445 Y. Leblanc, G. A. Dulk and J.-L. Bougeret (1998), Tracing the electron density from the
446 corona to 1 AU, *Sol. Phys.*, *183*, 165–180.
- 447 L. C. Lee and J. R. Jokipii (1975), Strong scintillations in astrophysics: I: The Markov
448 approximation, its validity and application to angular broadening, *Astrophys. J.*, *196*,
449 695–707.
- 450 P. K. Manoharan, M. Kojima and H. Misawa (1994), The spectrum of electron density
451 fluctuations in the solar wind and its variations with solar wind speed, *J. Geophys. Res.*,
452 *99*, 23411–23420.
- 453 D. B. Melrose, Plasma emission mechanism for Type I solar radio emission, *Solar Phys.*,
454 *67*, 357–375.

- 455 C. Mercier, P. Subramanian, A. Kerdraon, M. Pick, S. Ananthakrishnan and P. Janardhan
456 (2006), Combining visibilities from the giant meterwave radio telescope and the Nancay
457 radio heliograph. High dynamic range snapshot images of the solar corona at 327 MHz,
458 *Astron. Astrophys.*, *447*, 1189–1201.
- 459 G. Newkirk (1961), The solar corona in active regions and the thermal origin of the slowly
460 varying component of solar radio radiation, *Astrophys. J.*, *133*, 983–1013.
- 461 B. J. Rickett (1977), Interstellar scattering and scintillation of radio waves, *Ann. Rev.*
462 *Astron. Astrophys.*, *15*, 479–504.
- 463 A. C. Riddle (1974), On the observation of scattered radio emission from sources in the
464 solar corona, *Solar Phys.*, *35*, 153–169.
- 465 P.A. Robinson and I.H. Cairns (1998), Fundamental and harmonic emission in type III
466 solar radio bursts: I. Emission at a single location or frequency, *Sol. Phys.*, *181(2)*, 363.
- 467 S. R. Spangler (2002), The amplitude of magnetohydrodynamic turbulence, *Astrophys.*
468 *J.*, *576*, 997–1004.
- 469 S. R. Spangler and T. Sakurai (1995), Radio interferometer observations of solar wind
470 turbulence from the orbit of HELIOS to the solar corona, *Astrophys. J.*, *445*, 999–1016.
- 471 J.-L. Steinberg, M. Aubier-Giraud, Y. Leblanc and A. Boischot (1971), Coronal scattering,
472 absorption and refraction of solar radiobursts in the solar wind, *Astron. Astrophys.*, *10*,
473 362–376.
- 474 G. Thejappa and M. R. Kundu (1992), Unusually low coronal radio emission at the solar
475 minimum, *Solar Phys.*, *140*, 19–39.
- 476 P. Zlobec, M. Messerotti, G. A. Dulk and T. Kucera (1992), VLA and Trieste observations
477 of type I storms, type IV and pulsations, *Solar Phys.*, *141*, 165–180.

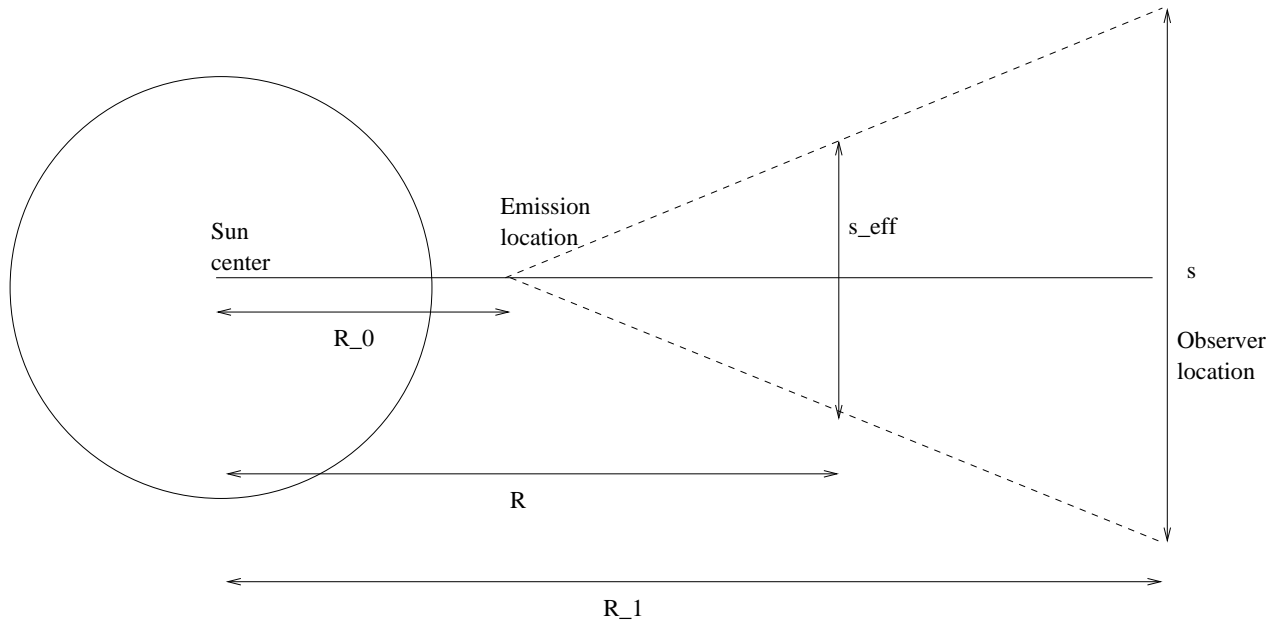


Figure 1. Geometry for spherically diverging wavefront, which is appropriate to a situation where the source is embedded in the scattering medium

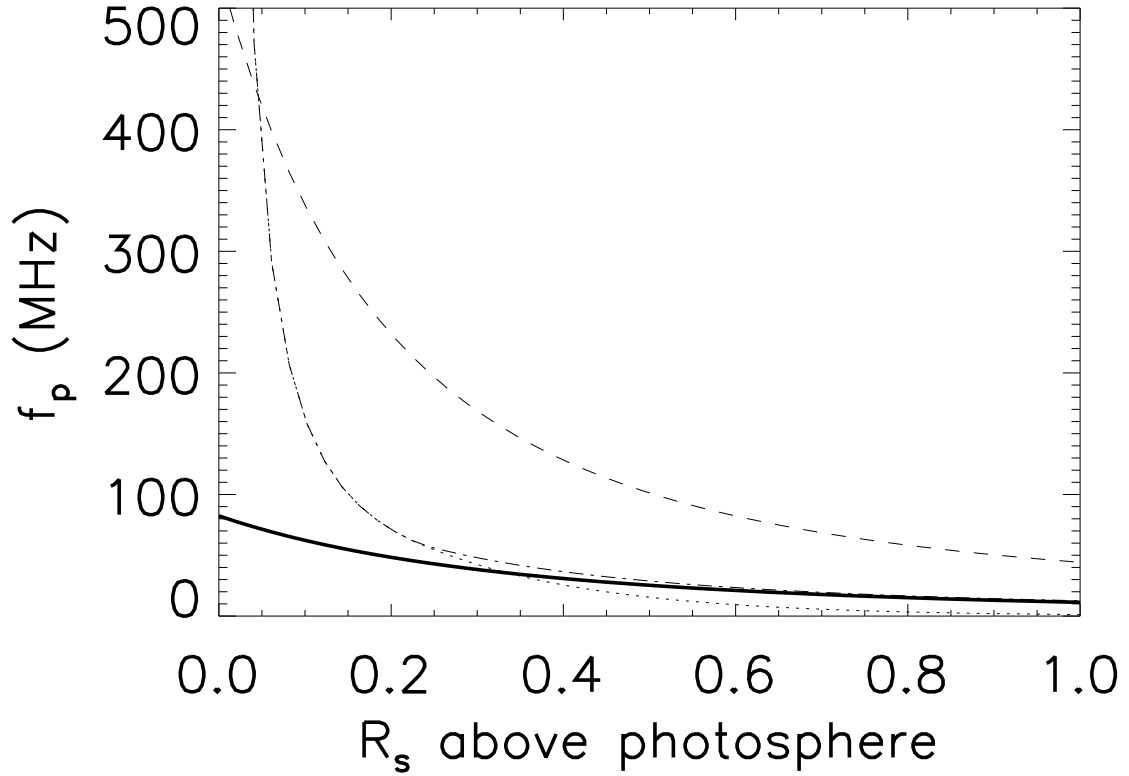


Figure 2. The plasma frequencies predicted by the four density models in the text are plotted against the height $h = R - R_{\odot}$ above the photosphere (in units of R_{\odot}). The solid line uses the Leblanc et al model (15), the dotted line uses the Aschwanden & Benz model (16), the dashed line uses the 4*Newkirk model (14) and the dash-dot line uses the “hybrid” model (17).

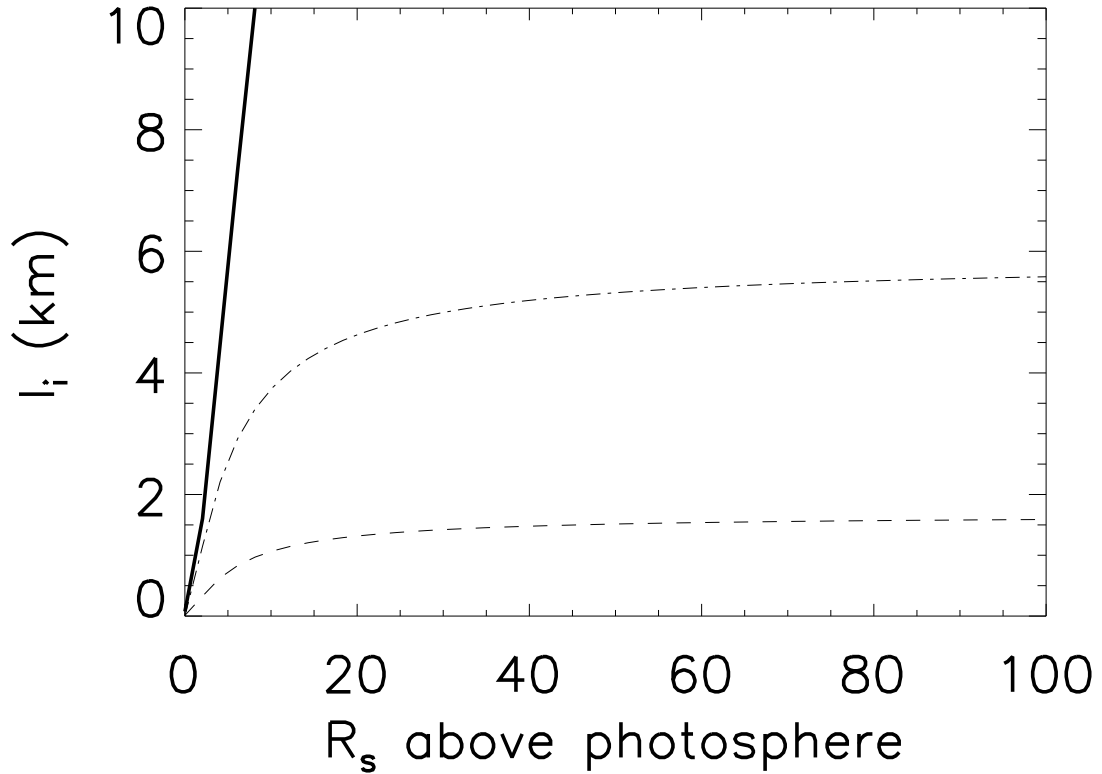


Figure 3. The inner scales (in units of km) predicted by some density models in the text are plotted against the height $h = R - R_{\odot}$ above the photosphere (in units of R_{\odot}). The solid line uses the Leblanc et al model (15), the dashed line uses the 4*Newkirk model (14), and the dash-dot line uses the hybrid model (17).

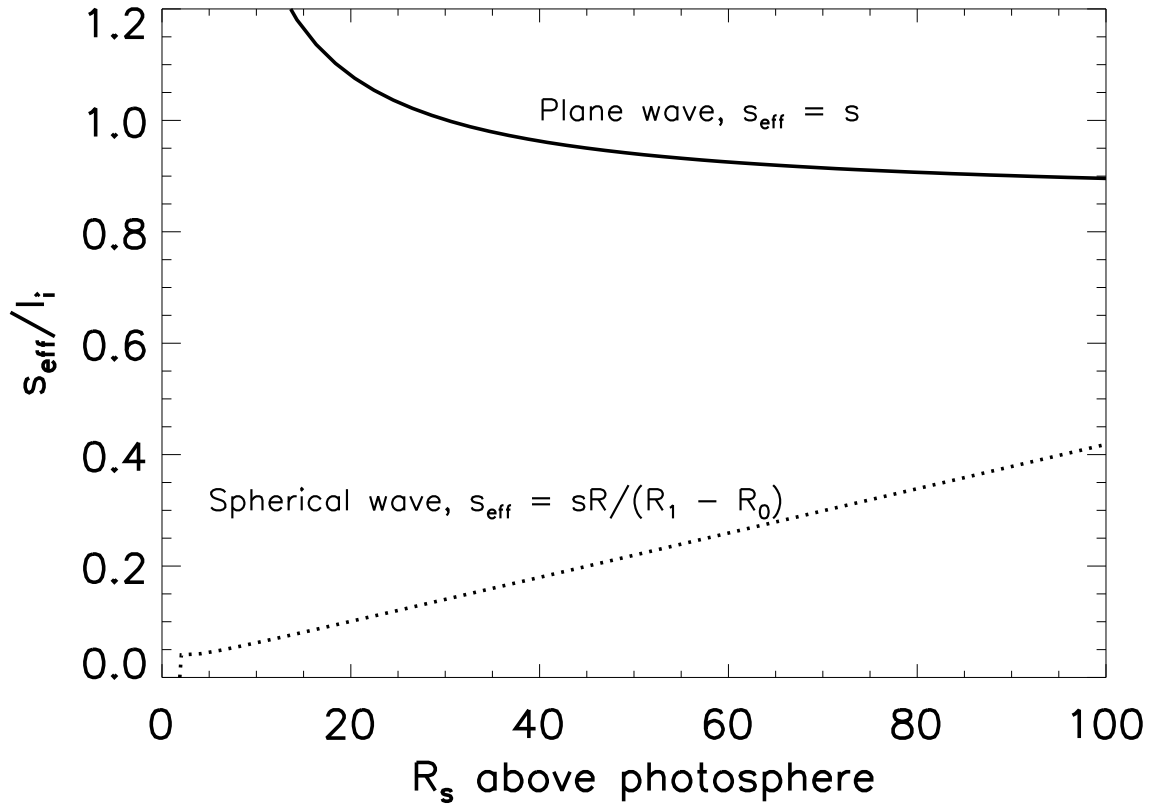


Figure 4. The ratio s_{eff}/l_i is plotted against the height $h = R - R_{\odot}$ above the photosphere (in units of R_{\odot}). The solid line shows the ratio for plane wave propagation (i.e., with $s_{\text{eff}} = s$), while the dotted line shows the ratio for spherical wave propagation (i.e., with $s_{\text{eff}} = sR/(R_1 - R_0)$). The hybrid density profile is used for determining the density and the inner scale.

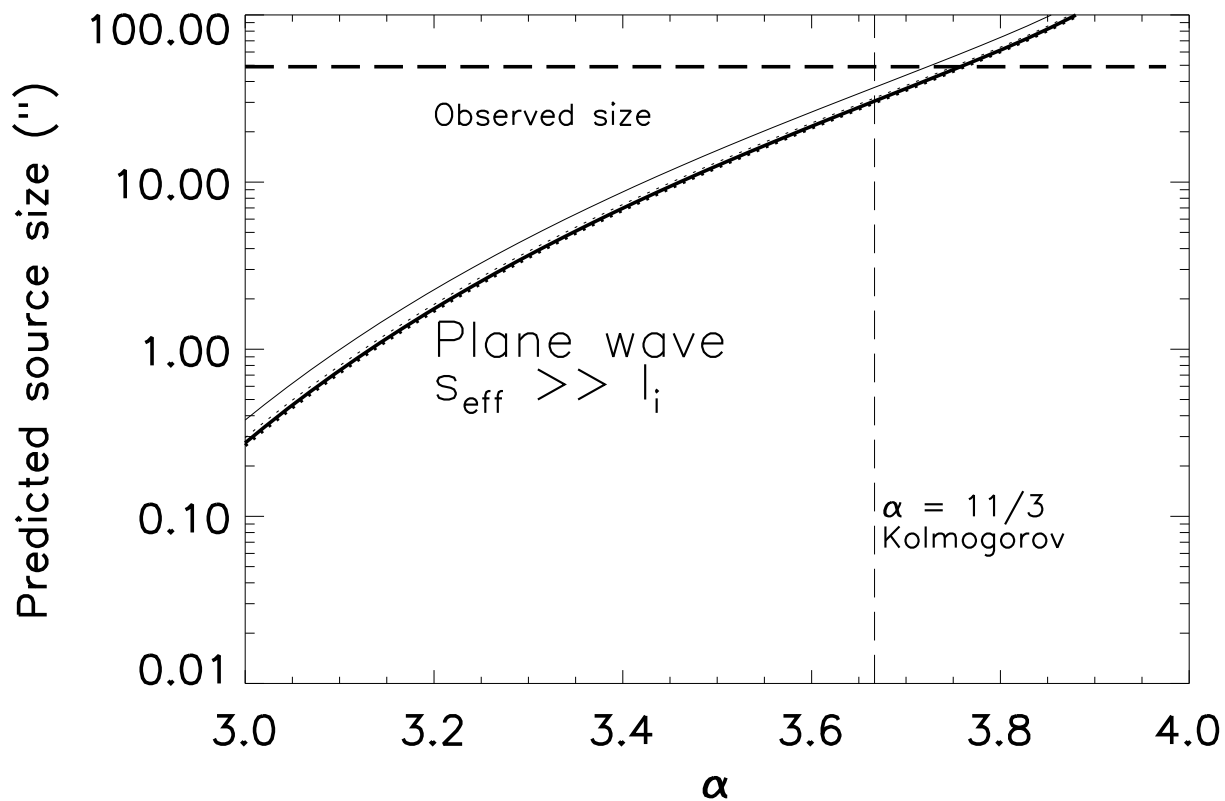


Figure 5. Predicted θ_c (1 AU) in " at 327 MHz for plane wave propagation, as a function of α , using (6), (10) and (13). The observed source size is 49". The thin line is for fundamental emission and the thick line is for second harmonic emission.

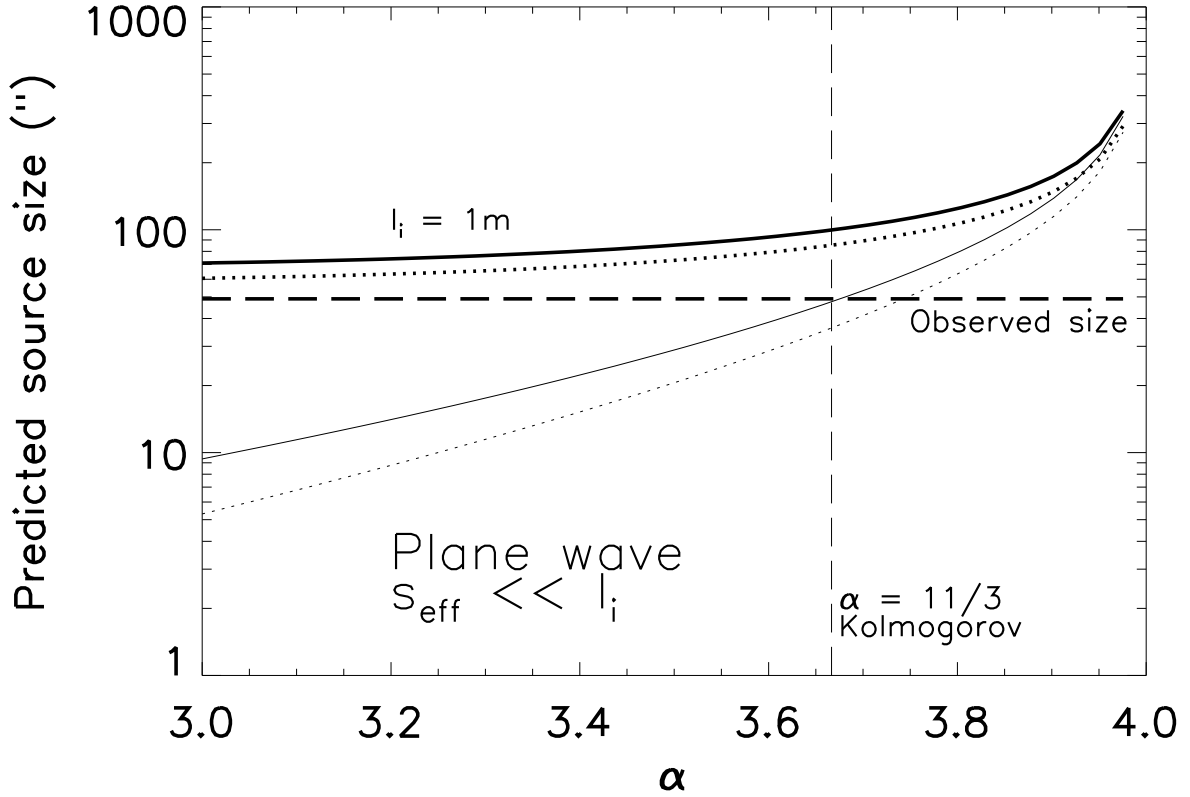


Figure 6. Predicted θ_c (1 AU) in " at 327 MHz for plane wave propagation as a function of α , using Eqs (7), (10) and (13). The solid line is for fundamental emission and the dotted line is for second harmonic emission. The heavy lines are computed with l_i set at an artificially low value of 1 m, while still using branch (7).

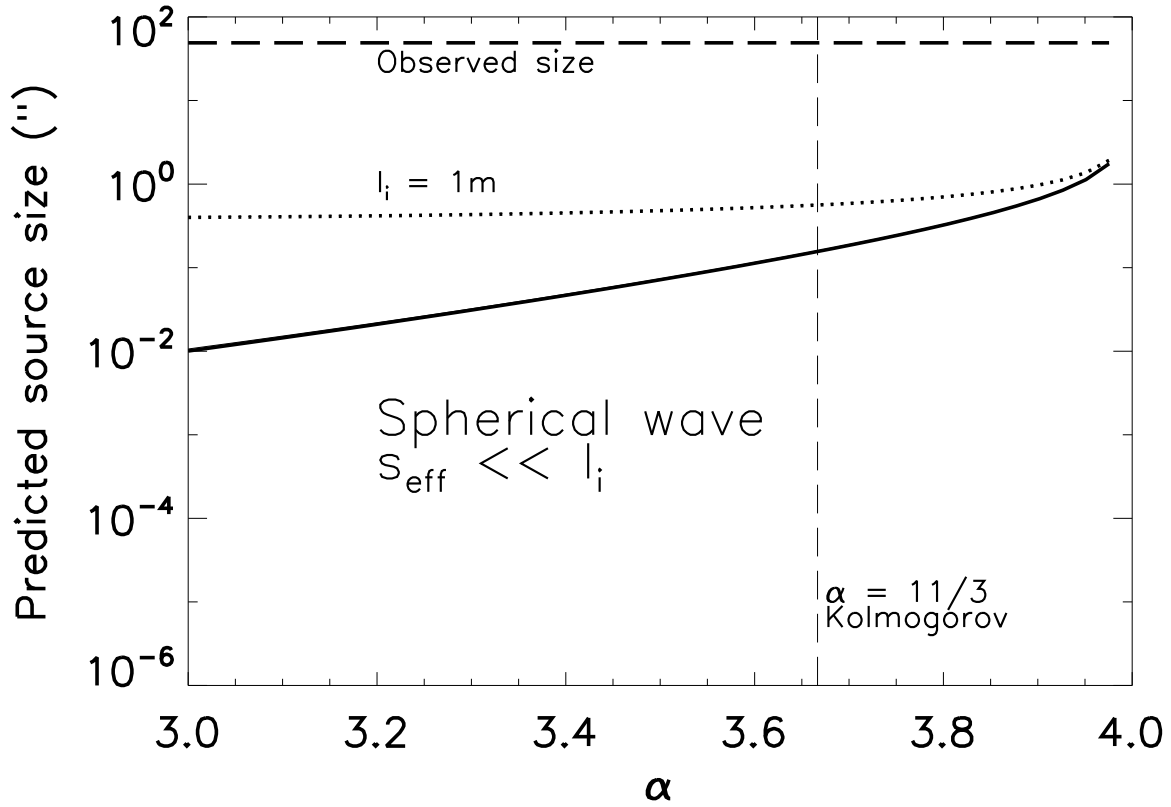


Figure 7. Predicted θ_c (1 AU) in " at 327 MHz for spherical wave propagation as a function of α , using (7), (11) and (13). The observed source size at 327 MHz is 49". There is negligible difference between fundamental and second harmonic emission. The solid lines are computed with l_i from prescription (4), while the dotted lines are computed with l_i set to an artificially low value of 1 m, while still using branch (7).

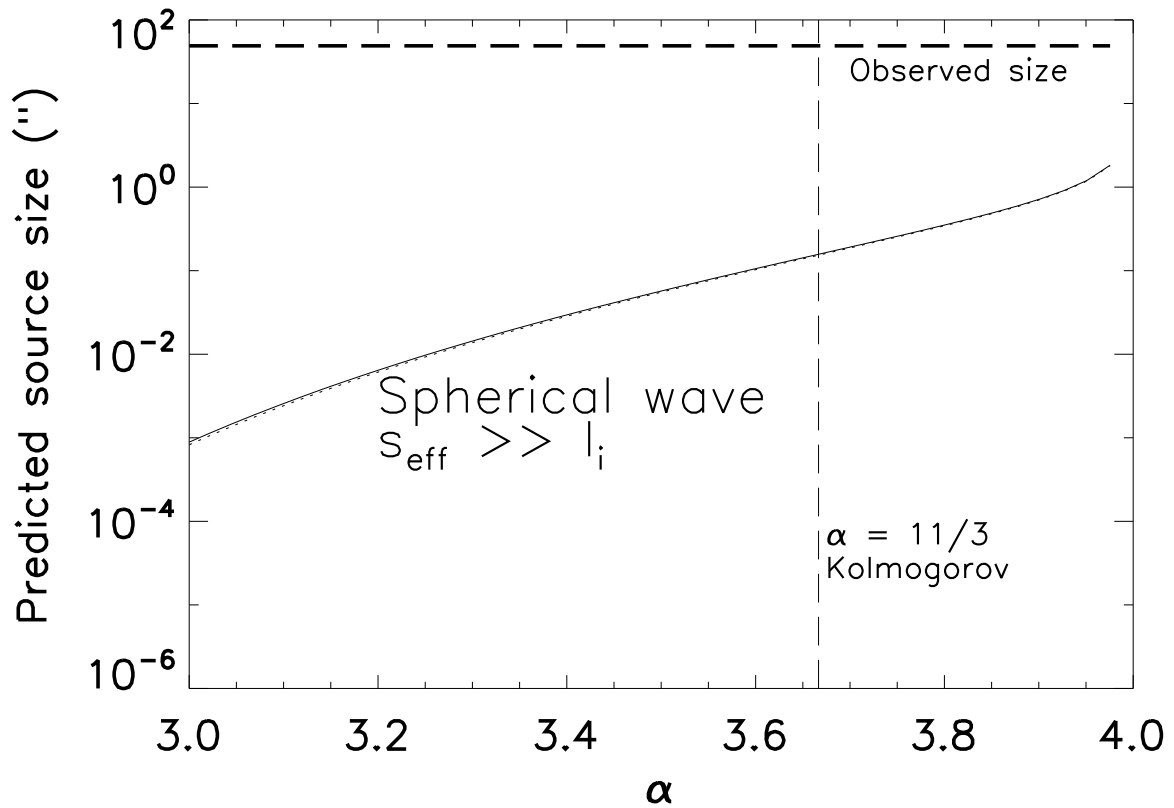


Figure 8. Predicted θ_c (1 AU) in " at 327 MHz for spherical wave propagation as a function of α , using (6), (11) and (13).. The difference between the predictions for fundamental and second harmonic emission is negligible.

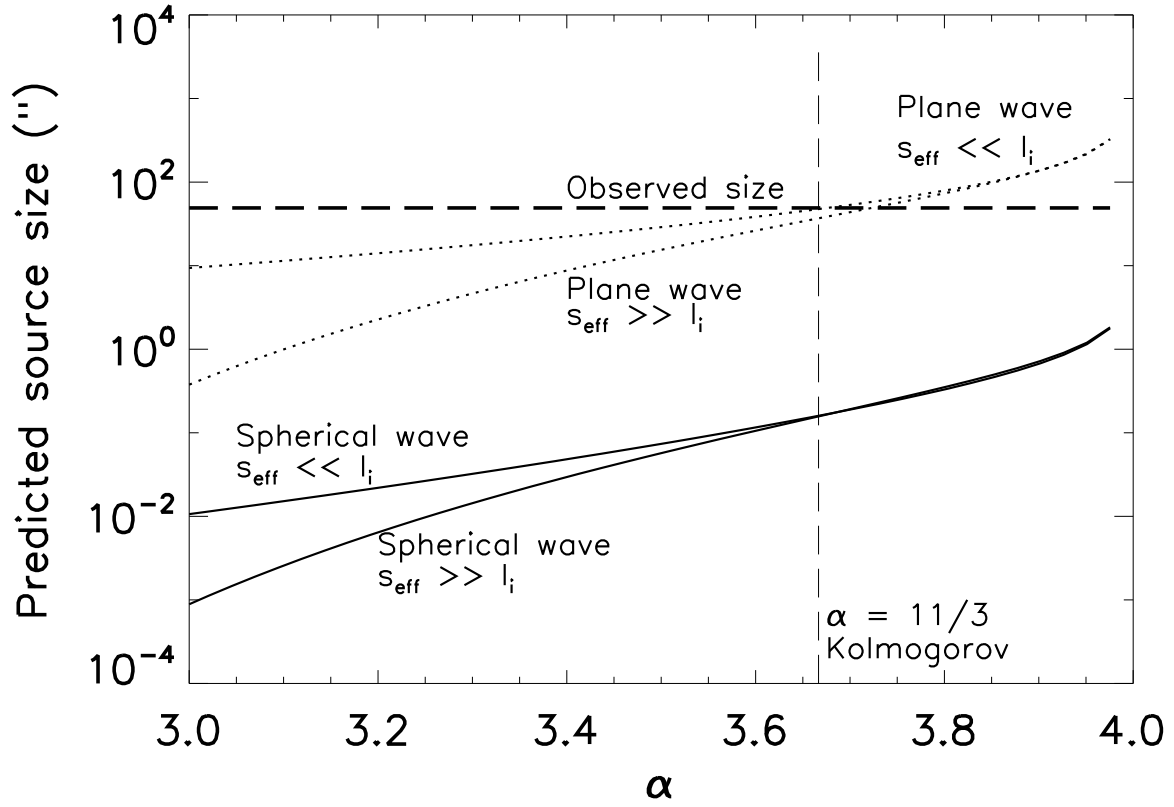


Figure 9. Direct comparison of θ_c (1 AU) for spherical (solid lines) and plane wave (dotted lines) propagation. Fundamental emission is assumed.